# Switchable two-dimensional electrides: A first-principles study

Xuhui Yang,[1,2] Kevin Parrish,[2] Yan-Ling Li,[3] Baisheng Sa,[1] Hongbing Zhan,[1] and Qiang Zhu[2,*]

[1]*College of Materials Science and Engineering, Fuzhou University, Fuzhou, Fujian Province, 350108, People's Republic of China*

[2]*Department of Physics and Astronomy, University of Nevada, Las Vegas, Nevada 89154,USA*

[3]*Laboratory for Quantum Design of Functional Materials, School of Physics and Electronic Engineering, Jiangsu Normal University, 221116, Xuzhou, People's Republic of China*

(Received 4 September 2020; accepted 17 February 2021; published 2 March 2021)

Electrides, with excess anionic electrons confined in their empty space, are promising for uses in catalysis, nonlinear optics, and spin electronics. However, the application of electrides is limited by their high chemical reactivity. In this paper, we report a group of chemically stable monolayer electrides with the presence of switchable nearly free electron (NFE) states in their electronic structures. Unlike conventional electrides, which are metals with floating electrons forming the bands crossing the Fermi level, the switchable electrides are semiconductors holding the NFE states close to the Fermi level. According to a high-throughput search, we identified 11 candidate materials with low-energy NFE states that can likely be exfoliated from the known layered materials. Under external strain, these NFE states, stemming from the surface image potential, will be pushed downward to cross the Fermi level. The critical semiconductor-metal transition can be achieved by a strain within 10% in several monolayer materials. These switchable electrides may provide an ideal platform for exploring quantum phenomena and modern electronic device applications.

DOI: 10.1103/PhysRevB.103.125103

## I. INTRODUCTION

Electrides are a class of unconventional compounds that contain excess valence electrons confined in the void or interlayer space that play the role of anions [1]. Chemically, such materials could serve as strongly reducing agents or catalysts for chemical syntheses. From a physics point of view, the confined electrons form (partially occupied) bands close to the Fermi level, which could lead to a dramatically reduced work function and high electric conductivity. These attractive physical and chemical properties collectively promise technological applications such as the splitting of carbon dioxide at room temperature [2], synthesis of ammonia from atmospheric nitrogen [3], and many others [4]. Recently, it was also proposed that the confined electrons in the electrides could be investigated for a role in topological phase transitions [5–8]. In the past, a number of electride materials have been investigated, both experimentally and computationally. Depending on the connectivity of crystal cavities and channels, the identified electrides could be classified as zero, one, and two dimensions (0D, 1D, and 2D). Of them, the 2D electride materials [9,10], with anionic electrons distributed in the 2D space, are of great interest since they are naturally connected with 2D material physics [11]. Indeed, the recent report on the synthesis of the monolayer $Ca_2N$ (exfoliated from the parent layered form) has driven electride research into the nanoregime [12]. The monolayer $Ca_2N$, by combining high surface areas of 2D materials with the exotic properties of anionic electrons, is favorable for applications as a transparent conductor in the modern electronic devices [11,12].

Despite the many unique properties that the floating anionic electrons bring, they also result in poor stability at room temperature and ambient atmosphere, which significantly limit the utilization of electrides as materials. In electride design, the conventional wisdom is to search for candidates with unpaired electrons present in their crystal voids [13–16]. In the band structure, these confined electrons form the distinct interstitial bands crossing the Fermi level. To date, most known electrides are strongly reducing metals due to the presence of these characteristic bands. Consequently, they are unstable in water and air. From an application perspective, it is desirable to have the material remain stable under normal conditions and switch to the electride phase under the operation. Therefore, an ideal material should be semiconducting with the lowest conduction bands occupied by the interstitial electrons. Under the working condition, the interstitial band can be then downshifted to the Fermi level. As such, the electride material will be maximally protected before it is in use, and the interstitial band can act as an effective transport agent in electronic devices. To achieve this goal, the key is to identify the materials that can hold an interstitial band close to the Fermi level.

In many known electrides, the interstitial electrons follow the nearly free electron (NFE) model in which the electrons are considered as plane-waves that are weakly perturbed by the periodic lattice potential. The dispersion can be roughly described by a paraboliclike dispersion of $E = \hbar^2 k^2/2m$. While the NFE states can be found in 3D systems, it is more natural to study them in 2D materials [17–20]. To date, many previous studies demonstrate that the NFE states are

*qiang.zhu@unlv.edu

 

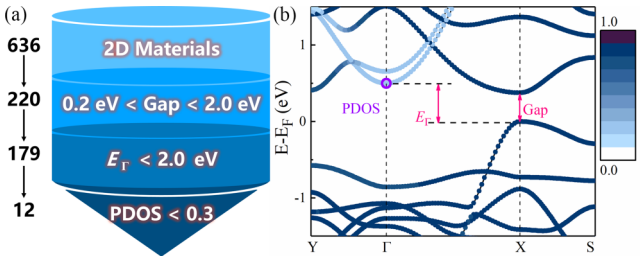


FIG. 1. Summary of the workflow. (a) Computational scheme for the screening of two-dimensional (2D) switchable electrides. (b) The definition of physical quantities used in the screening. The projected density of states (PDOS) denotes the ratio of densities which can be projected to the atomic orbitals. If the densities cannot be projected to any atomic orbitals, it suggests the electrons are loosely bound with the nucleus.

several electronvolts above the Fermi level. The high-energy NFE states require common band structure engineering approaches, such as chemical-electron doping [21,22], strain engineering [23–25], and electric fields [20,26–32], to lower their energy levels. It was only recently reported that the NFE states can be energetically found near the Fermi levels in a hypothetical compound $Sc_2C(OH)_2$ with its conduction band occupied by the NFE states 0.45–0.94 eV above the Fermi level [33,34]. The authors further proposed that the NFE states can be downshifted by external electric fields [34]. However, such switchable electrides have not been reported based on any known material.

In this paper, we present an automated workflow that can on-screen the potential switchable electrides in the monolayer forms. Our initial results revealed that around 10 candidate materials with low-energy NFE states can likely be exfoliated from the known layered materials. Under external strain, they will turn to the electride phases due to the downshifting of these NFE states. The critical semiconductor-metal transition can be achieved by a strain within 10% in several monolayer materials. The identification of such switchable electrides may provide an ideal platform for exploring novel quantum phenomena and modern electronic device applications.

## II. HIGH-THROUGHPUT SCREENING STRATEGY

In total, 636 2D candidates from material databases were investigated based on the four steps of screening, as shown in Fig. 1. The first step was to obtain potential 2D insulators or semiconductors from the online database [35]. For each 2D material, we performed density functional theory (DFT) calculations using a projector augmented wave method [36] as implemented in the VASP code [37]. The exchange and correlation potentials were treated with the generalized gradient approximation as proposed by Perdew-Burk-Ernzerhof (PBE) [38]. Preparation of input parameters and data extraction was done with the Pymatgen package [39]. A plane-wave cutoff energy of 700 eV was employed. The relaxation convergence criteria were $10^{-6}$ eV for energy and 0.01 eV/Å for force. In the relaxation, static, and nonself-consistent calculations, the reciprocal density was set to be 300. To avoid the interlayer interaction due to periodic boundary conditions, a vacuum layer of at least 15 Å thickness was added to each simulation at the screening stage. In the electronic band structure calculation, both PBE and Heyd-Scuseria-Ernzerhof (HSE) functionals [40] were used. The second step was to extract the 2D semiconducting materials by applying a band gap restriction (between 0.2 and 2.0 eV). Steps 3 and 4 involve the identification of the NFE states. We filtered the materials with eigenstates at the Γ point ($E_\Gamma$) of the first conduction band that are less than 2.0 eV. To ensure the conduction bands held the true NFE states, we also checked that the majority of the projected density of states (PDOS) could not be projected to the atomic orbitals, similar to a recent paper [14]. If the PDOS value at Γ was smaller than 0.3, we considered it a potential NFE state. These screenings successfully identified 12 materials, as summarized in Table I. Finally, we recalculated their electronic structures with a higher precision under different applied strain with both standard PBE and hybrid functional, as shown in Table I.

TABLE I. The summary of 2D materials investigated in this paper. $E_{\rm NFE}$ denotes the lowest gap between the NFE states and the Fermi energy. $\epsilon_c$ denotes the critical biaxial compressive strain values to turn the material metallic. The exfoliation energies are extracted from the online database [35]. Since PbS did not show zero gap, even when put under up to a 20% strain, we did not show its $\epsilon_c$ value. N/A = not applicable.

| Material | Gap (eV) | $E_{\rm NFE}$ (eV) | VBM at Γ | $\epsilon_c$ | $\epsilon_{\text{c-HSE}}$ | $E_{\rm exfoliation}$ (meV/atom) |
|---|---|---|---|---|---|---|
| RbLiS | 1.228 | 1.228 | Yes | −13% | −15% | 94.14 |
| RbLiSe | 1.326 | 1.326 | Yes | −12% | −15% | 100.08 |
| KAgSe | 0.511 | 0.511 | Yes | −9% | −12% | 101.49 |
| $K_4HgAs_2$ | 0.793 | 0.793 | Yes | −12% | −16% | 107.36 |
| KMgSb | 0.905 | 0.905 | Yes | −9% | −13% | 110.65 |
| NaZnAs | 0.480 | 0.480 | Yes | −6% | −10% | 118.68 |
| NaZnP | 0.719 | 0.719 | Yes | −7% | −9% | 124.80 |
| $Na_2Pd_3O_4$ | 0.376 | 0.497 | No | −3% | −6% | 139.05 |
| PbS | 1.654 | 1.924 | No | N/A | N/A | 187.54 |
| $Na_3As$ | 0.285 | 0.285 | Yes | −6% | −10% | 250.04 |
| $Rb_2Te$ | 0.477 | 0.477 | Yes | −7% | −11% | 388.51 |
| SiS | 0.494 | 0.494 | Yes | −13% | −15% | N/A |

## III. RESULTS AND DISCUSSIONS

From the 12 identified materials, it is interesting to note that most of them have alkaline metals at the outermost layer of the slab, as shown in Fig. S1 [41]. This is expected since their valence electrons are much more weakly bound than those in the inner shells. To proceed, we first ruled out the materials with high exfoliation energies (PbS, $Na_3As$, and $Rb_2Te$). SiS was also skipped since this compound is from a theoretical prediction [42]. Then we applied a series of biaxial strains on the remaining compounds. Below, we will discuss how to modulate the NFE states by strain engineering on two representative materials: $Na_2Pd_3O_4$ and NaZnAs.

### A. $Na_2Pd_3O_4$: An indirect band gap 2D electride

Figure 2 displays the changes of the electronic band structures of $Na_2Pd_3O_4$ under different strains. The pristine monolayer $Na_2Pd_3O_4$ is a semiconductor with a direct gap of

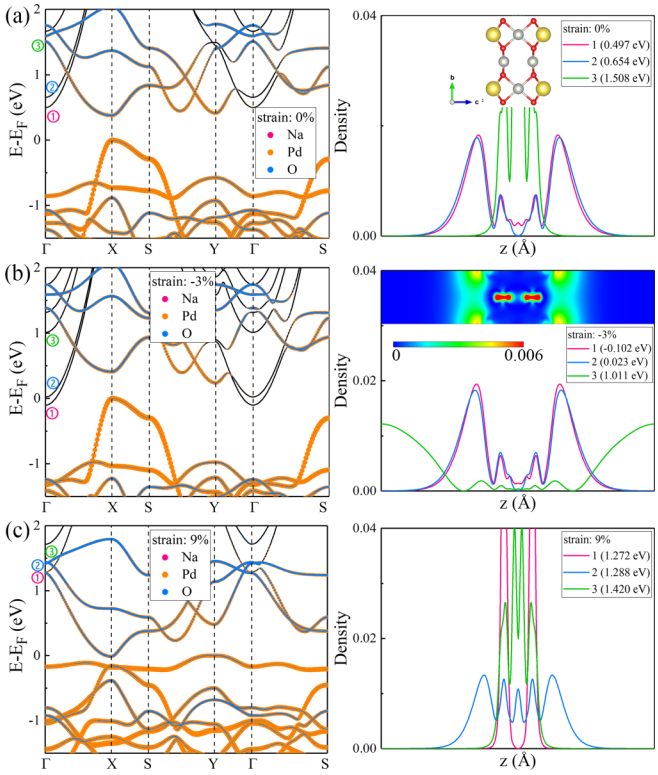


FIG. 2. The electronic structures of monolayer $Na_2Pd_3O_4$. (a)–(c) show the band structures and corresponding electron densities at the Γ point with 0%, −3%, and 9% strains. In the left column, each energy band is colored by the atoms which hold the largest portion of projected density of states (PDOS). If it cannot be projected to any atomic site, this corresponds to nearly free electron (NFE) states, as denoted by black color. The right columns display the partial charge density distributions of the three lowest conduction bands at the Γ point along the $z$ axis. The band numbers correspond to the circled numbers in the left columns. The side views of the structural model are shown in (a) as the inset. The Na, Pd, and O atoms are denoted by yellow, gray, and red spheres, respectively. The inset in (b) is the two-dimensional (2D) band decomposed charge density distribution of the lowest conduction band at the Γ point with the strain.

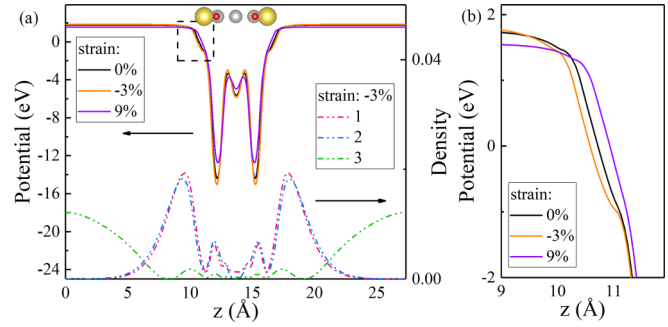


FIG. 3. The strain effects. (a) The calculated electrostatic potential (ESP) distribution of monolayer $Na_2Pd_3O_4$ with and without biaxial strains. The band decomposed charge density distribution at the Γ point of the first conduction band under −3% biaxial strain is also shown for comparison. The positions of each atom along the $z$ axis are shown as the inset. The Na, Pd, and O atoms are denoted by yellow, gray, and red spheres, respectively. (b) The enlarged detail of the dashed box in (a).

0.377 eV that has both the valence band maximum (VBM) and conduction band minimum (CBM) at the $X$ point (0.5, 0, 0). Not surprisingly, the system becomes metallic when the strains are applied. However, the behaviors drastically differ under different types of strains. Under tension, the band gap goes down continuously and becomes closed when it reaches 9% strain. On the other hand, compressive strain leads to a more dramatic change, and it needs only −3% strain to close the band gap. To understand the distinct behavior, we tracked the electronic band evolution and analyzed the characteristic wave functions under 0%, −3%, and 9% strains. As shown in Fig. 2(c), the dispersion of several conduction bands around the Γ point follows a paraboliclike relation. We also plotted the band decomposed charge density of the three lowest conduction bands (labeled from low to high) at the Γ point. Both bands 1 and 2 have four spikes. There are two smaller charge peaks at the oxygen nuclear sites, suggesting that O atoms can take some electrons since they are more electronegative than Na and Pd. More importantly, the majority of charges are symmetrically distributed outside the slab, confirming the presence of NFE states. With compression biaxial strain, the NFE states (0.497 eV at band 1 and 0.654 eV at band 2) drop more quickly than other conduction bands. At −3% strain, the CBM is shifted to the Γ point due to the lowered NFE states, while the original CBM state at the $X$ point remains intact. When tensile strains are applied, the semiconductor-metal transition follows a completely different path in which one nearly flat valence band moves upward, and the conduction bands are collectively pushed downward. Due to these joint efforts, the gap is finally bridged. However, it is notable that the NFE states actually take higher energies during the metallization process. The total evolution has been shown in Fig. S2 in the Supplemental Material [41].

The direction-dependent behavior can be understood by examining the nature of the NFE states. We first found that the bulk $Na_2Pd_3O_4$ did not exhibit low-energy NFE bands (Fig. S3 in the Supplemental Material [41]). Different from the bulk electrides in which the NFE states are occupying the crystal voids, the NFE states of 2D electrides stem from the image potential states. When the metal has a band gap near the vacuum level $E_{vacuum}$, an electron below $E_{vacuum}$ may be trapped in the potential well formed by the Coulomblike attractive image potential and the repulsive surface barrier [17,21,22,43]. Whether or not the electron can be trapped depends on the spatial distribution of the potential well. If the image potential has a long tail, the NFE states are more likely to be stabilized. Figure 3 displays the electrostatic potential (ESP) distribution of $Na_2Pd_3O_4$ under 0%, −3%, and 9% strains. Clearly, the tensile strain sharpens the ESP distribution compared with the pristine form. Thus, the NFE states under tension occupy higher energy levels than those in the pristine form. On the other hand, the compressive strain makes the ESP more extended. Consequently, the electrons can be trapped around the shoulder with a lower eigenvalue.

To check our DFT results, we also investigated the NFE states of the 1D electron model with an analytical potential well. Figure 4 shows the solved eigenstates for a potential with

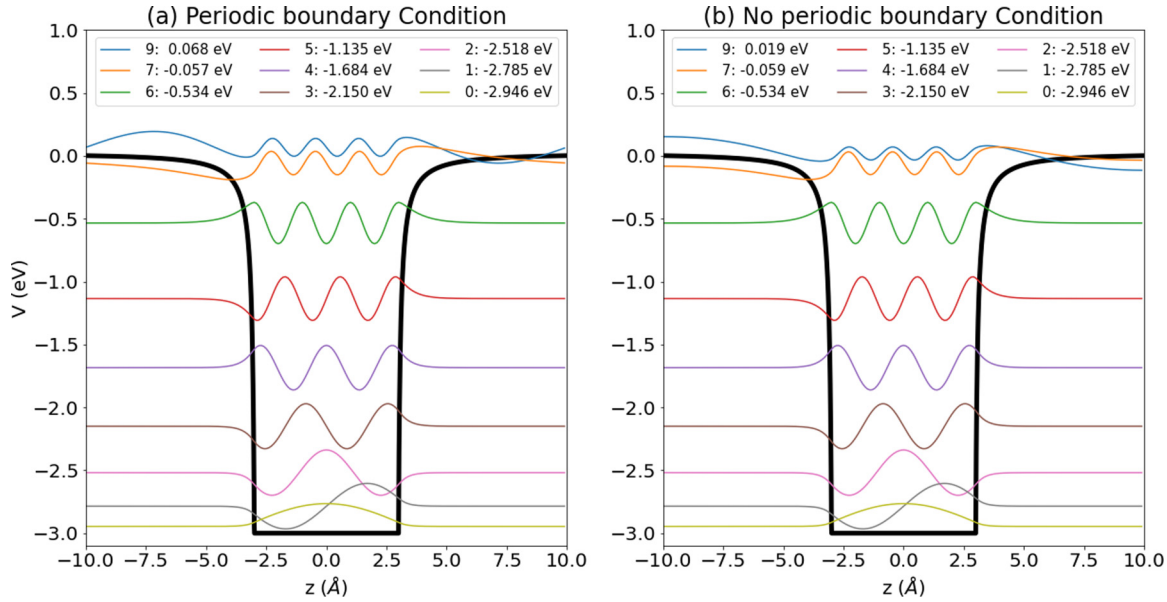


FIG. 4. The solution of a one-dimensional (1D) Schrödinger equation with an analytical potential (a) with and (b) without the periodic boundary condition. The thick black lines denote the potential, and the colored lines denote the wave functions corresponding to different energy levels. Note that energy levels 7 and 9 are the nearly free electron (NFE) states.

the following form:

$$V = \begin{cases} -3 & |z| <= a \\ -\frac{1}{4(z-a+\delta)} - \frac{1}{4(-z-a+\delta)} + \frac{1}{4(-2a+2L+\delta)} & |z| > a \end{cases},$$

where $a$ (5 Å) is slab size, $L$ (10 Å) is half the distance between two centers, and $\delta = \frac{1}{4V_0}$ (where $V_0 = -3$ eV). Figure 4 shows the solution of the 1D model at the given $V$ with and without the periodic boundary condition. Under the periodic boundary condition, each repeating unit has a thickness of 20 Å. From Fig. 4, it is clear that all wave functions and eigenvalues for the solutions that are trapped in the well (negative eigenvalues) are the same between the periodic and nonperiodic conditions. When the NFE states emerge, shown as 7 and 9 in Figs. 4(a) and 4(b), the results begin to differ.

Furthermore, we employed the DFT simulated potentials to check the corresponding eigenstates in the 1D electron models. Figure 5 shows the results of several low-energy NFE states for the given ESPs from DFT simulation at 0%, −3%, and 9% strains of monolayer $Na_2Pd_3O_4$. For each potential, we plot the first three NFE states, corresponding to energy levels 14, 15, and 16. While these NFE states have very similar shapes in their wave functions, the structures at −3% strain yield consistently smaller eigenvalues than those at 0% and 9% strains, which is consistent with our DFT results, as shown in Fig. 2. Therefore, we conclude that a negative biaxial strain can promote the activity of the NFE states by modifying the ESP distribution.

### B. NaZnAs: A direct band gap 2D electride

Different from $Na_2Pd_3O_4$, many materials in Table I have their VBM at the Γ point. For these materials, the semiconductor-to-metal transitions under strain become more complicated when the VBM and CBM directly meet each other. As shown in Fig. 6, the VBM states of pristine monolayer NaZnAs correspond to the $p_x/p_y$ orbitals of As (bands 1 and 2, see more details in Fig. S4 in the Supplemental Material [41]). The CBM at the Γ point of band 3 is 0.476 eV above the VBM. The decomposed charge density plot suggests that four competing maxima exist in band 3, with two corresponding to the NFE states and the other two corresponding to the electrons trapped by the As nucleus. Compared with band 1

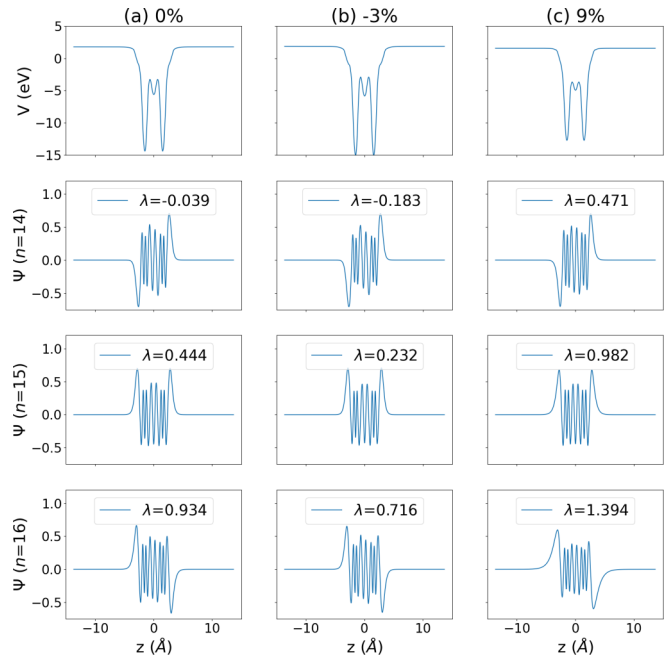


FIG. 5. The simulated nearly free electron (NFE) states for the given electrostatic potentials (ESPs) from density functional theory (DFT) simulation at 0%, −3%, and 9% strains of monolayer $Na_2Pd_3O_4$. The energy levels (λ) for the corresponding NFE states are given in eV.

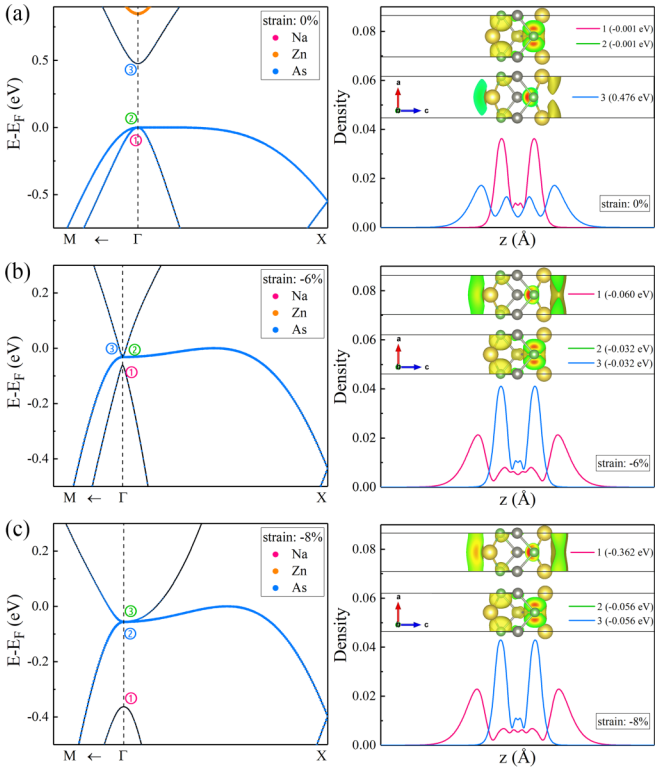


FIG. 6. The electronic structures of monolayer NaZnAs. The band structures under (a) 0%, (b) −6%, and (c) −8% biaxial strains. The right column plots the corresponding partial charge densities of three representative bands (two highest valence bands and one lowest conduction band) at the Γ point along the $z$ axis. For comparison, the isosurfaces of charge density plots for each band were also shown as the insets. The Na, Zn, and As atoms are denoted by yellow, gray, and green spheres, respectively.

of the $Na_2Pd_3O_4$ in Fig. 2(a), the dispersion of band 3 in Fig. 6(a) is less parabolic since it has more densities inside the slab. Clearly, the hybridization between the $p_x/p_y$ orbitals of As (bands 1 and 2) and the interstitial electrons dominate the electronic properties near the Fermi level. When put under compressive strain, the energy of NFE states gets closer to the Fermi level. Consequently, there is a prominent charge transfer from the $p_x/p_y$ orbitals of As to the interstitial electrons. When it reaches a critical strain near −6% [Fig. 6(b)], the charge transfer is complete, and the hybridization effect becomes negligible. Therefore, further application of strain leads to a quick downshift of the interstitial electrons [band 1 in Fig. 6(c)]. For instance, at −8% strain, the energy of interstitial electrons was reduced to −0.362 eV, while the Fermi level is occupied by the $p_x/p_y$ orbitals of As (bands 2 and 3). These phenomena suggest that 2D materials with low-energy NFE states can exhibit rich electronic behavior when their mechanical attributes are altered. In particular, the coexistence of the flat and NFE bands [Fig. 6(b)] may be useful for exploring quantum phenomena.

### C. Feasibility and possible verification

Introducing strains to 2D nanomaterials has been widely applied to tune the materials' properties [44]. To check the feasibility for possible experimental confirmation, we systematically investigated the stress-strain relations for all candidate materials in Table I. In total, five materials need a critical strain less than 10% to complete the semiconductor-metal transition. In Fig. 7, we plot the stress-strain relation for $Na_2Pd_3O_4$, NaZnAs, and the previously proposed $Sc_2C(OH)_2$. All strain values fall into the region of elastic deformation. Therefore, the transitions between the electride and nonelectride phase are likely reversible. Among them, the lowest critical strain is found to be −3% in the standard PBE functional for $Na_2Pd_3O_4$. When a more accurate hybrid functional is used, the critical strains systematically increase, as shown in Table I. This value is still high for practical application. However, the critical stress may be further reduced by chemical doping. Meanwhile, the energy of NFE states can be lowered by other means, such as external electric fields [34]. To date, none of these materials have been experimentally synthesized. Nevertheless, their parent bulk materials do exist. Exfoliating the 2D forms from their parent bulk materials requires energies between 90 and 130 meV/atom, which is higher than graphene (70 meV/atom) and $MoS_2$ (76 meV/atom) but comparable to $PtSe_2$ (111 meV/atom) [35,45]. We also noticed that several candidates were theoretically investigated for applications other than the electride properties [42,46,47]. While no single 2D switchable electride has been realized, this paper can undoubtedly facilitate this research by providing several candidate materials for experimental verification. If one of them can be made, the experimental verification should be straightforward.

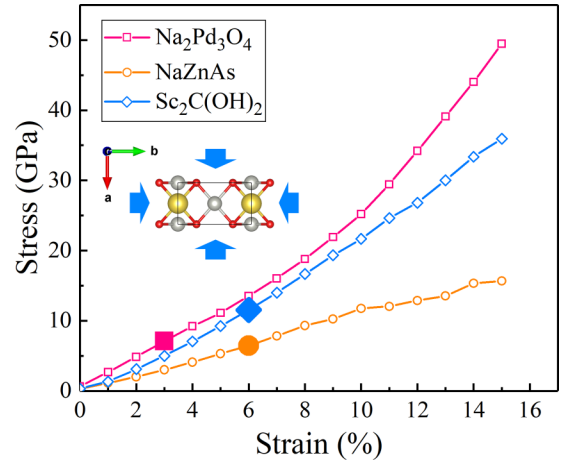


FIG. 7. Calculated stress-strain curves for three representative materials. The inset is the schematic diagram of biaxial compressive strain. The solid points denote the critical biaxial compressive strain values $\epsilon_c$ for the semiconductor-metal transition.

## IV. CONCLUSIONS

In summary, we report the computational design of switchable monolayer electrides from a high-throughput screening. From over 600 2D candidates which are potentially exfoliatable from the known materials, we found a family of candidates that may hold the required low-energy NFE states. Unlike the conventional bulk electrides or the recently synthesized 2D monolayer intrinsic electride $Ca_2N$, these monolayer

electrides are chemically stable semiconductors. Under a strain of $<10\%$, their NFE states can form the partially occupied bands crossing the Fermi level. Consequently, the reversible electride phase transition can be achieved via strain engineering. Thanks to the improved stability, these predicted materials are more amenable for fabrication and operation. They may find uses in switchable nanodevices or sensors for gas detection and electron transports.

## ACKNOWLEDGMENTS

Q.Z. and X.H.Y. acknowledge the use of computing resources from XSEDE (DMR180040). This paper was also supported by the National Natural Science Foundation of China (52073061, 51872048, 21973012, 11674131). The study of X.H.Y. at University of Nevada is supported by China Scholarship Council (CSC) No. 201806650022.

[1] J. L. Dye, Acc. Chem. Res. **42**, 1564 (2009).
[2] Y. Toda, H. Hirayama, N. Kuganathan, A. Torrisi, P. V. Sushko, and H. Hosono, Nat. Commun. **4**, 2378 (2013).
[3] M. Kitano, Y. Inoue, Y. Yamazaki, F. Hayashi, S. Kanbara, S. Matsuishi, T. Yokoyama, S.-W. Kim, M. Hara, and H. Hosono, Nat. Chem. **4**, 934 (2012).
[4] H. Hosono, J. Kim, Y. Toda, T. Kamiya, and S. Watanabe, Proc. Natl. Acad. Sci. **114**, 233 (2017).
[5] M. Hirayama, S. Matsuishi, H. Hosono, and S. Murakami, Phys. Rev. X **8**, 031067 (2018).
[6] H. Huang, K.-H. Jin, S. Zhang, and F. Liu, Nano Lett. **18**, 1972 (2018).
[7] C. Park, S. W. Kim, and M. Yoon, Phys. Rev. Lett. **120**, 026401 (2018).
[8] S.-C. Zhu, L. Wang, J.-Y. Qu, J.-J. Wang, T. Frolov, X.-Q. Chen, and Q. Zhu, Phys. Rev. Mater. **3**, 024205 (2019).
[9] K. Lee, S. W. Kim, Y. Toda, S. Matsuishi, and H. Hosono, Nature **494**, 336 (2013).
[10] T. Inoshita, S. Jeong, N. Hamada, and H. Hosono, Phys. Rev. X **4**, 031023 (2014).
[11] S. Zhao, Z. Li, and J. Yang, J. Am. Chem. Soc. **136**, 13313 (2014).
[12] D. L. Druffel, K. L. Kuntz, A. H. Woomer, F. M. Alcorn, J. Hu, C. L. Donley, and S. C. Warren, J. Am. Chem. Soc. **138**, 16089 (2016).
[13] T. Tada, S. Takemoto, S. Matsuishi, and H. Hosono, Inorg. Chem. **53**, 10347 (2014).
[14] L. A. Burton, F. Ricci, W. Chen, G.-M. Rignanese, and G. Hautier, Chem. Mater. **30**, 7521 (2018).
[15] Y. Zhang, H. Wang, Y. Wang, L. Zhang, and Y. Ma, Phys. Rev. X **7**, 011017 (2017).
[16] Q. Zhu, T. Frolov, and K. Choudhary, Matter **1**, 1293 (2019).
[17] V. M. Silkin, J. Zhao, F. Guinea, E. V. Chulkov, P. M. Echenique, and H. Petek, Phys. Rev. B **80**, 121408(R) (2009).
[18] X. F. Chen, J. S. Lian, and Q. Jiang, Phys. Rev. B **86**, 125437 (2012).
[19] N. T. Cuong, M. Otani, and S. Okada, J. Phys. Condens. Matter **26**, 135001 (2014).
[20] X. Yang, B. Sa, H. Zhan, and Z. Sun, J. Mater. Chem. C **5**, 12228 (2017).
[21] E. R. Margine and V. H. Crespi, Phys. Rev. Lett. **96**, 196803 (2006).
[22] S. Hu, J. Zhao, Y. Jin, J. Yang, H. Petek, and J. G. Hou, Nano Lett. **10**, 4830 (2010).
[23] Z. Ni, Q. Liu, K. Tang, J. Zheng, J. Zhou, R. Qin, Z. Gao, D. Yu, and J. Lu, Nano Lett. **12**, 113 (2012).
[24] S. Song, D. H. Keum, S. Cho, D. Perello, Y. Kim, and Y. H. Lee, Nano Lett. **16**, 188 (2016).
[25] C. R. Zhu, G. Wang, B. L. Liu, X. Marie, X. F. Qiao, X. Zhang, X. X. Wu, H. Fan, P. H. Tan, T. Amand, and B. Urbaszek, Phys. Rev. B **88**, 121301(R) (2013).
[26] H. Min, B. Sahu, S. K. Banerjee, and A. H. MacDonald, Phys. Rev. B **75**, 155115 (2007).
[27] K. F. Mak, C. H. Lui, J. Shan, and T. F. Heinz, Phys. Rev. Lett. **102**, 256405 (2009).
[28] Q. Liu, X. Zhang, L. Abdalla, A. Fazzio, and A. Zunger, Nano Lett. **15**, 1222 (2015).
[29] B. Ghosh, S. Nahas, S. Bhowmick, and A. Agarwal, Phys. Rev. B **91**, 115433 (2015).
[30] L. Debbichi, O. Eriksson, and S. Lebègue, J. Phys. Chem. Lett. **6**, 3098 (2015).
[31] A. Ramasubramaniam, D. Naveh, and E. Towe, Phys. Rev. B **84**, 205325 (2011).
[32] X. Dai, W. Li, T. Wang, X. Wang, and C. Zhai, J. Appl. Phys. **117**, 084310 (2015).
[33] M. Khazaei, A. Ranjbar, M. Ghorbani-Asl, M. Arai, T. Sasaki, Y. Liang, and S. Yunoki, Phys. Rev. B **93**, 205125 (2016).
[34] J. Zhou, M. Khazaei, A. Ranjbar, V. Wang, T. D. Kühne, K. Ohno, Y. Kawazoe, and Y. Liang, J. Mater. Chem. C **8**, 5211 (2020).
[35] K. Choudhary, I. Kalish, R. Beams, and F. Tavazza, Sci. Rep. **7**, 5179 (2017).
[36] P. E. Blöchl, Phys. Rev. B **50**, 17953 (1994).
[37] G. Kresse and J. Furthmüller, Phys. Rev. B **54**, 11169 (1996).
[38] J. P. Perdew, K. Burke, and M. Ernzerhof, Phys. Rev. Lett. **77**, 3865 (1996).
[39] S. P. Ong, W. D. Richards, A. Jain, G. Hautier, M. Kocher, S. Cholia, D. Gunter, V. L. Chevrier, K. A. Persson, and G. Ceder, Comput. Mater. Sci. **68**, 314 (2013).
[40] A. V. Krukau, O. A. Vydrov, A. F. Izmaylov, and G. E. Scuseria, J. Chem. Phys. **125**, 224106 (2006).
[41] See Supplemental Material at http://link.aps.org/supplemental/10.1103/PhysRevB.103.125103 for a detailed description of atomic structures of all 12 materials from the high-throughput screening, band structures of bulk and monolayer $Na_2Pd_3O_4$, and band structures of NaZnAs, $Sc_2C(OH)_2$, and other materials.
[42] J.-H. Yang, Y. Zhang, W.-J. Yin, X. Gong, B. I. Yakobson, and S.-H. Wei, Nano Lett. **16**, 1110 (2016).
[43] U. Höfer, I. Shumay, C. Reuß, U. Thomann, W. Wallauer, and T. Fauster, Science **277**, 1480 (1997).
[44] S. Deng, A. V. Sumant, and V. Berry, Nano Today **22**, 14 (2018).
[45] Y. Wang *et al.*, Nano Lett. **15**, 4013 (2015).
[46] Q. Wang, J. Li, Y. Liang, Y. Nie, and B. Wang, ACS Appl. Mater. Interfaces **10**, 41670 (2018).
[47] X. Zhang, C. Liu, Y. Tao, Y. Li, Y. Guo, Y. Chen, X. C. Zeng, and J. Wang, Adv. Funct. Mater. **30**, 2001200 (2020).